Computational assessment of detailed soot formation models in ethylene/air laminar diffusion flames

Sebastián Ruiz, Cesar Celis, Luís Fernando Figueira da Silva

Computational assessment of soot models in ethylene/air laminar diffusion flames

Sebastian Ruiz, Cesar Celis[1]

Mechanical Engineering Section, Pontificia Universidad Católica del Perú
Av. Universitaria 1801, San Miguel, 15088, Lima, Peru

Luís Fernando Figueira da Silva

Institut Pprime, CNRS, ISAE-ENSMA, Université de Poitiers
1 avenue Clément Ader, Futuroscope Chasseneuil 86961, France

[1] Corresponding author – Tel.: +51 1 626 2000 / 4870
E-mail address: ccelis@pucp.edu.pe (C. Celis)

Abstract

To improve the accuracy of soot formation and evolution predictions, several physical and chemical models have been developed over the last decades. These models include (i) detailed chemical kinetic mechanisms describing both gas-phase chemistry related to combustion processes and reaction pathways leading to large-sized aromatic molecules, which are needed for modeling soot formation, and (ii) soot models providing a comprehensive description of soot particle dynamics and interactions with gas-phase chemical species. Accordingly, in this work, two detailed soot models, the method of moments (MOM) and the discrete sectional method (DSM), are evaluated in ethylene/air laminar diffusion flames, and their corresponding results are compared with experimental measurements. Furthermore, the NBP and KM2 chemical kinetic mechanisms are assessed and compared with each other by examining key chemical species related to soot formation and evolution. To compute gas mixture's radiative properties, the weighted sum of gray gases model considering a gray medium is also utilized. Finally, the contributions of the soot precursors known as PAH (polycyclic aromatic hydrocarbon) to soot formation are also analyzed. The main results show that the discrepancies in PAH concentrations obtained with different chemical kinetic mechanisms can be significant. In addition, compared to MOM ones, DSM results obtained here show a better agreement with experimental data. Finally, the analysis of PAH shows that those with two (A2) to four (A4) aromatic rings impact the most on soot modeling. Specifically, contributions of A4 were found to be more significant at lower heights above the burner, whereas A2 was found to be more impactful downstream as the flame develops. Maximum contributions of A2 and A4 to the soot inception rate were 66% and 85%, respectively, whereas the maximum summed contribution of PAH with five (A4R5) to seven (A7) aromatic rings accounted for only 13% of the inception rate.

Keywords: Soot formation, Polycyclic aromatic hydrocarbons, Laminar flames, Chemical kinetic mechanisms, Non-premixed flames.

Nomenclature

Variables

a	Absorption coefficient
b	Soot absorption model constant
d	Diameter
D_s	Diffusion coefficient
G_r	Coagulation source term
k_B	Boltzmann constant
m_c	Mass of one carbon atom
M_r	Moment of order r
n	Number density function
N_A	Avogadro number
$N_{C,P}$	Number of carbon atoms
R_r	Inception source term
T	Temperature
v	Velocity
W_r	Surface growth and oxidation source term
$Y_{soot,i}$	Section i soot mass fraction

Greek-letter variables

β	Collision frecuency function
γ	Sticking coefficient
ρ	Density
φ	Transported scalar
Γ	Diffusivity

Abbreviations

CFD	Computational fluid dynamics
DOM	Discrete ordinate method
DSM	Discrete sectional method

HAB	Height above the burner
HACA	Hydrogen-abstraction acetylene-addition
LBL	Line-by-line
LII	Laser-induced incandescence
MOM	Method of moments
MOMIC	Method of moments with interpolative closure
NBKD	Narrow band k distribution
OTA	Optically thin approximation
PAH	Polycyclic aromatic hydrocarbon
PBE	Population balance equation
PLIF	Planar laser induced fluorescence
PSDF	Particle size distribution function
RTE	Radiative transfer equation
UDF	User-defined function
UDS	User-defined scalar
UDM	User-defined memory
URF	Under-relaxation factor
WSGG	Weighted sum of gray gases
SVF	Soot volume fraction

1 Introduction

Particulate matter emissions from combustion processes have been demonstrated to significantly change our environment. Soot and the aromatic molecules associated with its formation are well known for their harmful effects on both health and the biosphere [1,2]. However, the generation of soot particles has also practical applications, such as enhancing heat transfer in furnaces and producing carbon-derived nanomaterials [3]. Soot related research is thus motivated by the need to address this substance's negative and positive aspects.

Soot formation and evolution is often studied in laminar flame configurations because they are not as experimentally/computationally intricate as turbulent flames, and because they include the physical and chemical phenomena associated with soot particle formation [4]. Accordingly, the modeling of soot formation and evolution in laminar flames typically involves the use of a gas-phase chemical kinetic mechanism, a soot model, and a radiation one. In recent decades, research on soot modeling has focused on developing more accurate and detailed models for each of these three coupled processes.

Chemical kinetic mechanism developments have focused on extending existing kinetic mechanisms to describe larger polycyclic aromatic hydrocarbons (PAH). For instance, the KAUST Mechanism 2 (KM2) [5] was developed based on a previously developed mechanism including a detailed description of aliphatic species chemistry, and further extended to describe PAH growth pathways in more detail. To reduce the associated computational costs, research on kinetic mechanisms has also focused on reducing the kinetic mechanism accounting for a particular reactive flow configuration [5,6]. Although this may seem contradictory at first, the point of reducing a mechanism is not to neglect the description of large PAH, but rather to cut reaction pathways that are not relevant to the particular reactive flow configuration considered. For instance, Selvaraj et al. [6] developed a kinetic mechanism that initially contained 397 chemical species and reduced it to 99 species while still describing PAH growth up to coronene ($C_{24}H_{12}$). In their work, they reported a relatively good agreement in terms of PAH concentrations when compared to a detailed kinetic mechanism.

State-of-the-art soot models, including those based on the method of moments (MOM) or the discrete sectional method (DSM) based ones, involve parameters related to the morphology of soot particles, such as particle diameter and particle size distribution

(PSDF). These models mainly differ in their ability to accurately describe the PSDF. Both model families have been successfully employed to describe the distribution and amount of soot generated in laminar flames. For example, Wang et al. [5] reproduced experimental soot volume fractions for a series of ethylene laminar counterflow flames using a MOMIC (MOM with interpolative closure) model. Additionally, using a DSM model, Zhang and coworkers [7] replicated soot volume fraction measurements for a jet fuel laminar flame. Detailed soot models also include the modeling of chain-like structured soot aggregates [8,9]. In MOM models this is usually accomplished by defining the transported moments as a two-variable function, whereas in sectional ones particles and aggregates are discretized and transported in different sections. Additionally, a coagulation mechanism describing the formation of aggregates needs to be included, and the mathematical formulation of the mechanisms related to soot evolution and soot diffusion needs to be adapted [10,11]. Therefore, the modeling of aggregates usually implies a higher level of complexity.

Regarding radiation transport, although detailed models describing the radiative properties for the entire spectrum exist, such as the line-by-line (LBL), they are not usually considered when modeling multidimensional flames. This is due to the high computational cost that they usually imply. Instead, more simplified models are generally employed [9,12]. These can be divided into spectral models, such as the optically thin approximation (OTA) and the narrow-band based models, and global models, such as the weighted sum of gray gas (WSGG) and its variants. The OTA model is only suitable for describing flames where radiation self-absorption is not significant [13]. The classical WSGG model [14] has the limitation of being accurate only for specific species concentration ratios and a certain range of pressures and temperatures. However, different approaches based on the WSGG, such as the superposition weighted sum of gray gas model (SWGG), enable it to be applied to arbitrary gas mixtures [15]. Narrow band k-distribution based models are in turn the most accurate among these models, but they also require both the solution of the radiative properties for each spectral band accounted for, and the use of a detailed radiative database [16]. In these models indeed, except for the OTA model, the radiation intensity needs to be calculated to obtain the self-absorption term, which is solved by the radiative transport equation (RTE). Several approaches are commonly used to solve the RTE, some of which include spherical harmonics (SHM), discrete-ordinate methods (DOM), and Monte-Carlo statistical ones [12]. In particular, soot radiative properties are usually determined assuming that they are in the Rayleigh's

regime, thus neglecting scattering and obtaining a correlation for the soot absorption coefficient by means of the soot volumetric fraction [13].

Computational cost is typically the main concern when modeling soot formation and evolution in laminar flames. For instance, a chemical kinetic mechanism requires solving a transport equation for each chemical species, meaning that for a mechanism featuring 100 species, the mechanism will usually require solving 99 or 100 transport equations, depending on the mass conservation approach. Additionally, as highlighted by Quadarella et al. [17], a soot model is usually developed by considering a specific chemical kinetic mechanism. This means that, when using soot models with different kinetic mechanisms, the soot model parameters often require readjustment. Similarly, different soot models involve different computational costs. In particular, MOM-based models generally involve the solution of a few transport equations only, usually between 3 to 6 depending on the MOM variant and on the accuracy needed [18,19]. DSM, in turn, requires a transport equation for each (volume) section considered, whose number typically ranges from 25 to 35, and which doubles when soot aggregation modeling is accounted for [11,20]. Another aspect to consider when selecting a soot model is its complexity. Indeed, the MOM with interpolative closure (MOMIC) model has been widely used, in particular due to its relative ease of implementation [6,18,21–23].

Inception of soot particles is of paramount importance in the modeling of soot, because it involves the coupling of the gas-phase chemical species and the solid incipient particles [24]. When using MOM or DSM-based models, two approaches employed to model soot inception involve (i) the combination of PAH by dimerization, and (ii) the collision and union of PAH of different sizes. Inception by dimerization is usually modeled as a two-step process in which the dimerization rate is first determined, and the inception rate is computed from both the dimerization rate and the PAH dimer concentration [25]. In turn, the collision and union of PAH follows the ideal gas collision theory formulation for two molecules. Although there is a consensus on the need to consider PAH molecules as soot precursors in soot inception modeling [26,27], there is no general agreement on which of these two formulations is the most adequate, and even more so, which particular molecules from the PAH pool must be accounted for. Generally, works using MOM based models [19,23] employ the inception formulation given by Blanquart and Pitsch [25], which describes the dimerization process of either pyrene or PAH of different sizes. However, some works employing MOM use as well the homogenous and heterogenous combination of PAH formulation [22,28,29]. In turn,

recent research works using discrete sectional methods usually model the inception as the collision and combination of PAH with five aromatic rings [9,11,30–32]. It is also worth noticing here the PAH availability in the chemical kinetic mechanisms employed. For instance, kinetic mechanisms describing PAH growth up to pyrene only limit the inception modeling to either the collision or dimerization of pyrene or other relatively small-size PAH [33].

Accordingly, in this work, two detailed soot models, MOMIC [34], a particular variant of the MOM based ones, and DSM [35,36] are applied to model ethylene/air laminar diffusion flames and their corresponding results are compared with experimental measurements. The main contributions of this work include the comparisons of both detailed chemical kinetic mechanisms (NBP and KM2) and detailed soot models (MOMIC and DSM), as well the analysis of soot precursors, in particular PAH, and their role in determining the level of soot formed in laminar flames. Other contributions of this work relate to the fact that to the best of our knowledge this is the first time that, using user-defined scalars (UDS) and user-defined functions (UDF), these two detailed soot models have been implemented in the general-purpose software ANSYS Fluent (Release 23.1). This means that all model details have been first properly formulated and then coded in a programming language readable by the computational tool employed here. The remainder of the article is organized as follows. Section 2 describes the mathematical model utilized here. In Section 3, in turn, the numerical model, including the flame configuration accounted for, is highlighted. Finally, Sections 4 and 5 discuss the main results obtained here and the conclusions drawn from them, respectively.

2 Mathematical Formulation

In this section the flame configuration and the mathematical models used in this work are discussed. More specifically, the transport equations, kinetic mechanisms, soot formation and evolution and radiation models required to solve the combustion system and characterize it are briefly described.

2.1 Flame Configuration

This work involves the study of an atmospheric pressure laminar ethylene/air diffusion flame. The burner used to characterize this flame, one of the target flames in the

Laser-Induced Incandescence (LII) Workshop from 2005, is a Gülder type. This type of burner allows stabilizing a flame that generates relatively high amounts of soot. The burner consists of two coaxial tubes, with the inner tube featuring a diameter of 11 mm for the fuel inlet and the outer one having a diameter of 100 mm for the airflow. The fuel flow rate is 0.1 slpm, whereas the air flow rate is set to 60 slpm. The experimental data used for comparison and validation purposes here was obtained by Jerez et al. [32], in which soot-related properties were measured using simultaneous LII and planar laser-induced fluorescence (PLIF) techniques. A two color pyrometry technique was also used for the measurements of temperature fields.

2.2 Governing Equations

Transport equations for mass, momentum, energy and chemical species are solved accounting for both a laminar flow with variable density and a 2-D axisymmetric reference frame. Finite-rate chemistry is employed, meaning that each chemical species mass fraction transport equation is solved. Chemical species' mass diffusivity is computed based on averaged mixture properties following Fick's law. Mixture-averaged viscosity and thermal conductivity are solved based on the mixture temperature and Leonard-Jones parameters of each chemical species. Thermal diffusion, also known as Soret effect, is neglected in this work. In addition, enthalpy transport due to species mass diffusion is accounted for in the energy equation. Finally, gravitational effects are considered in the momentum transport equation.

2.3 Chemical Kinetic Mechanisms

Chemical kinetic mechanisms specify, along with their associated thermodynamical and transport properties, the gaseous chemical species and chemical reactions accounted for in the numerical simulations carried out. Two chemical kinetic mechanisms are evaluated here, (i) the one developed by Narawasyamy et al. [37], commonly known as NBP mechanism, and (ii) the Kaust Mech 2 (KM2), developed by Wang et al. [5].

The NBP mechanism was validated for a wide range of fuels, ranging from methane to iso-octane and accounting for both premixed and diffusion laminar flames. This mechanism describes the formation of PAH up to benzo[gui]fluranthene ($C_{18}H_{10}$), a 5-ringed aromatic molecule.

In turn, the KM2 mechanism features 202 gaseous chemical species and 1351 chemical reactions. In this case, the reaction pathways leading to the formation of benzene are taken from the USCII mechanism [38], which was validated for fuels featuring 1 to 4 carbons in its fundamental structure. Additionally, this kinetic mechanism improves the description of cyclopentadienyl (C_5H_5) related reactions, which are important for the formation of non-planar PAH structures. KM2 describes the formation of PAH up to coronene ($C_{24}H_{12}$), a 7-ringed aromatic molecule.

The modeling of soot inception in soot models is inherently limited by the number and size of the PAH accounted for in the kinetic mechanisms. Therefore, when using the NBP mechanism, modeling of inception is usually done by means of benzene (C_6H_6), naphthalene ($C_{10}H_8$), or pyrene ($C_{16}H_{10}$) [39,40]. However, when using the KM2 mechanism, soot inception considers larger PAH, including benzo[ghi]pyrene (BAPYR), a 5-ringed molecule, coronene (A7), a 7-ringed molecule, and other large-sized aromatic molecules [22].

2.4 Soot Modeling

Two different modeling approaches describing the formation and evolution of soot sphere particles are compared in this work, (i) the method of moments with interpolative closure (MOMIC) [34] and (ii) the discrete sectional method (DSM) [35,36]. These particular model variants have been considered here because, in addition to their relative ease of implementation, they are representative of different ways used to describe the essence of detailed soot formation and evolution mechanisms. In particular, these two soot models predict the soot particle size distribution (PSDF), which is relevant to soot formation and evolution mechanisms, to determine the soot surface area, the soot surface growth and oxidation. The main differences between the two soot models studied here come from the way in which they both solve the PSDF and model the associated soot formation and evolution mechanisms.

Accordingly, first, the method of moments reconstructs the PSDF by determining its statistical moments [41]. In other words, each moment is related to a statistical parameter of the particle size distribution, i.e., mean, variance, and skewness. The main feature of this model relates to the fact that, to model the PSDF, it usually employs a few moments only. Thus only a few additional transport equations need to be solved. In particular, the MOMIC variant accounted for here considers the formation of spherical particles only,

i.e., a univariate approach is taken. More specifically, in the MOMIC model implemented in this work, three statistical moments are transported, and a logarithmic Lagrange interpolation is used to close the associated source terms. Accordingly, each moment is defined in terms of the mass as follows,

$$M_r = \sum_{i=1}^{\infty} {m_i}^r N_i \,, \tag{1}$$

where M_r is the r-th statistical moment of the soot PSDF, and m_i and N_i are the mass and number density of the ith size class, respectively. The corresponding transport equation for the r-th statistical moment is expressed as follows,

$$\nabla \cdot (\rho \bar{v})\, M_r = \nabla \cdot (\rho D_s \nabla M_r) + \frac{dM_r}{dt}\,, \tag{2}$$

where D_s is the diffusion coefficient for laminar flames, and $\frac{dM_r}{dt}$ is the r-th statistical moment source term. Following the work by Zimmer and Pereira [42], a constant value of 10^{-6} m^2/s^2 is considered for D_s. Source terms are defined in turn in terms of the soot formation and evolution mechanisms,

$$\frac{dM_r}{dt} = R_r + G_r + W_r, \tag{3}$$

where R_r, G_r, and W_r are the inception, surface growth, and oxidation source terms, respectively. Particularly, the soot particle inception is modeled here as the collision and union of pyrene (A4) molecules as follows,

$$R_0 = \gamma \sqrt{\frac{4\pi k_B T}{m_C N_{C,P}}} (dN_A)^2 [PAH]^2, \tag{4}$$

$$R_r = 2 N_{C,P} R_{r-1}, \tag{5}$$

where γ is the sticking coefficient, k_B is the Boltzmann constant, T is the temperature, m_C the mass of a single carbon atom, $N_{C,P}$ the number of carbon atoms in the PAH, N_A the Avogadro number, and $[PAH]$ is the PAH mole concentration. Notice that the sticking coefficient accounts for a collision efficiency between soot precursors [25]. Soot surface growth and oxidation mechanisms are modeled here based on the hydrogen abstraction acetylene addition (HACA) mechanism, using the Arrhenius parameters proposed by Appel et al. [43]. The formulation of these source terms is described in detail in the work

by Frenklach and Wang [44]. Empirical parameters used in the referred formulation include the steric factor, which accounts for the fraction of active sites available for chemical reactions in the soot particle surface, and a collision efficiency for the OH oxidation process [43]. Previous analyses of these empirical parameters showed that the sticking coefficient (related to collision efficiency) directly affects the quantity of soot formed, whereas the steric factor can affect the soot volume fraction fields [45]. Accordingly, in order to match the experimental peak values, both γ and steric factor are prescribed here as being equal to 0.001 and 1, respectively.

The second model considered, discrete sectional method (DSM), computes the PSDF by directly dividing it into a finite number of sections, where a transport equation is solved for each section. In this work, only the formation of spherical particles is accounted for. In addition, the particle size distribution is divided into 30 volume sections, where each section is represented by its mean particle volume. Accordingly, in terms of the soot mass fraction, the transport equations solved in each section are expressed as,

$$\nabla \cdot (\rho \vec{v})\, Y_{soot,i} = \nabla \cdot \left(\rho D_s \nabla Y_{soot,i}\right) + \dot{\omega}_{soot,i}\,, \tag{6}$$

where $Y_{soot,i}$ stands for the soot mass fraction of section i, D_s is the diffusion coefficient, and $\dot{\omega}_{soot,i}$ is the soot mass fraction section source term. This source term is defined in turn as,

$$\dot{\omega}_{soot,i} = \rho_s\left(\delta_{1,i}\dot{Q}_{i,nuc} + \dot{Q}_{i,SG} + \dot{Q}_{i,Ox} + \dot{Q}_{i,Cond}\right), \tag{7}$$

where ρ_s is the soot density and $\dot{Q}_{i,nuc}$, $\dot{Q}_{i,SG}$, $\dot{Q}_{i,Ox}$ and $\dot{Q}_{i,Cond}$ correspond to the inception, surface growth, oxidation and condensation source terms, respectively. $\delta_{1,i}$ is in turn the Kronecker delta function, meaning that the inception source term is only introduced in the first section [46].

Similar to the MOMIC, each section source term in the DSM is defined in terms of the soot associated mechanisms. Indeed, when using the NBP mechanism, the inception and condensation modeling is effected using pyrene, whereas, when using KM2, inception and condensation source terms are modeled based on PAH of different sizes, ranging from phenanthrene (A2) to coronene (A7). More specifically, in the DSM, accounting for the PAH listed in Table 1, the inception and condensation source terms are defined respectively as,

$$\dot{Q}_{1,nuc} = \sum_{j=1}^{N_{PAH}} \sum_{k=j}^{N_{PAH}} \gamma\, V_{PAH} \sqrt{\frac{4k_B T}{m_{PAH}}}\, (dN_A)^2\, [PAH]_j [PAH]_k, \tag{8}$$

$$\Delta\dot{Q}_{i,cond} = \sum_{j=1}^{N_{PAH}} \gamma_{cond}\, V_{PAH,j}\, \left([PAH]_j N_A\right) \int_{V_i}^{V_{i+1}} \beta_{i,PAH}\, n(V) dV, \tag{9}$$

where V_{PAH} and d are the total volume and diameter of the two colliding PAH, respectively. N_{PAH} is the total number of PAH considered in inception and m_{PAH} is the reduced mass of the two colliding PAH. Additionally, in Eq. (8), γ_{cond} is the condensation collision efficiency, set to 1 here, $\beta_{i,PAH}$ is the collision frequency function, and $n(V)$ is the presumed profile of the soot number density, whose definitions are available in [47]. Like the MOMIC model, to describe the soot surface reaction mechanisms, the DSM also uses a HACA formulation. The same Arrhenius parameters given by Appel et al. [43] are also utilized in this case. Finally, the empirical parameters include as well a sticking coefficient, a steric factor, and a OH oxidation collision efficiency, which are set to the same values as in the MOMIC model.

Table 1. PAH species accounted for in the inception of soot particles.

PAH species	Formula
Naphtalene (A2)	$C_{10}H_8$
Acenaphtylene (A2R5)	$C_{12}H_8$
Pyrene (A4)	$C_{16}H_{10}$
Cyclopenta[cd]pyrene (A4R5)	$C_{18}H_{10}$
Benzo(a)pyrene (Bapyr)	$C_{20}H_{12}$
Benzo(ghi)perylene (Bghiper)	$C_{22}H_{12}$
Coronene (A7)	$C_{24}H_{12}$

2.5 Radiation Modeling

The radiation model used in this work to solve the radiative transfer equation (RTE) is the discrete ordinate method (DOM). DOM discretizes the RTE in a finite number of direction vectors in the angular space for which the radiation intensity is computed. A gray gas-based approach is considered in this work, where scattering phenomena are neglected, and equivalent radiation properties through the entire spectrum are computed. More precisely, the weighted sum-of-gray-gases (WSGG) model [14] is used to compute the gas mixture's emissivity and absorption coefficients. When using the WSGG model, fictitious gases are used to represent the mixture radiation effects, whose model coefficients are calculated based on the concentration of the participating species, that is CO_2 and H_2O, and the temperature of the medium. The soot absorption coefficient is in turn determined as

$$a_s = b_1 \rho Y_s \cdot [1 + b_T (T - 2000)], \tag{10}$$

where ρ is the gas mixture density, Y_s the soot mass fraction, T the temperature, and b_1 and b_T are model coefficients set equal to 1232.4 m^2/kg and 4.8E-4 K^{-1}, respectively. The values of these coefficients were obtained by Sazhin [48] based on the assumption that soot absorption weighting coefficients are a function of temperature [49]. Finally, the total absorption coefficient is obtained as the sum of both the gas mixture and soot absorption coefficients. Both DOM and WSGG models have been used in previous works where it has been shown that they predict relatively well radiative heat transfer and temperature distributions [45, 46].

3 Numerical Model

In this section, the numerical model used to predict soot formation and evolution in the particular laminar flame accounted for here is described. First, the computational domain and mesh are specified. Then, the solver and numerical schemes utilized here are highlighted. Finally, the implementation of soot models carried out in this work is briefly described.

3.1 Computational domain, boundary conditions, and mesh refinement

The computational domain geometry and the initial computational mesh were generated using the ANSYS Design Modeler and ANSYS Meshing modules, respectively. As highlighted in Fig. 1, the computational domain is delimited in the radial direction by the burner's outer diameter, resulting in a radius of 50 mm. In the axial direction, in turn, to permit the development of the duct boundary layer and the flame, a sufficiently extended domain height of 150 mm was accounted for. The initial computational mesh featured about 20,000 elements, where fine elements were located near the burner walls and the flame centerline, and over the burner surface.

The boundary conditions accounted for here are also shown in Fig. 1. Following previous works [52,53], the outer side of the computational domain is represented here by a wall. The boundary condition imposed on this wall is defined by a zero-shear stress and a constant ambient temperature. Thus, neither hydrodynamic nor thermal boundary layers are formed in this region. At the burner duct walls in turn, a no-slip wall condition and a linear temperature distribution in the axial direction, increasing from 300 to 400 K, are imposed. The former wall boundary condition enables the formation of a developed flow in the fuel feed tube, and the latter one considers preheating effects in this tube, which were previously studied in the work by Guo et al. [52]. At both fuel and air inlets, both a uniform velocity and a flow temperature of 300 K are prescribed. Additionally, the outflow is defined by a pressure outlet condition, where the atmospheric pressure is set.

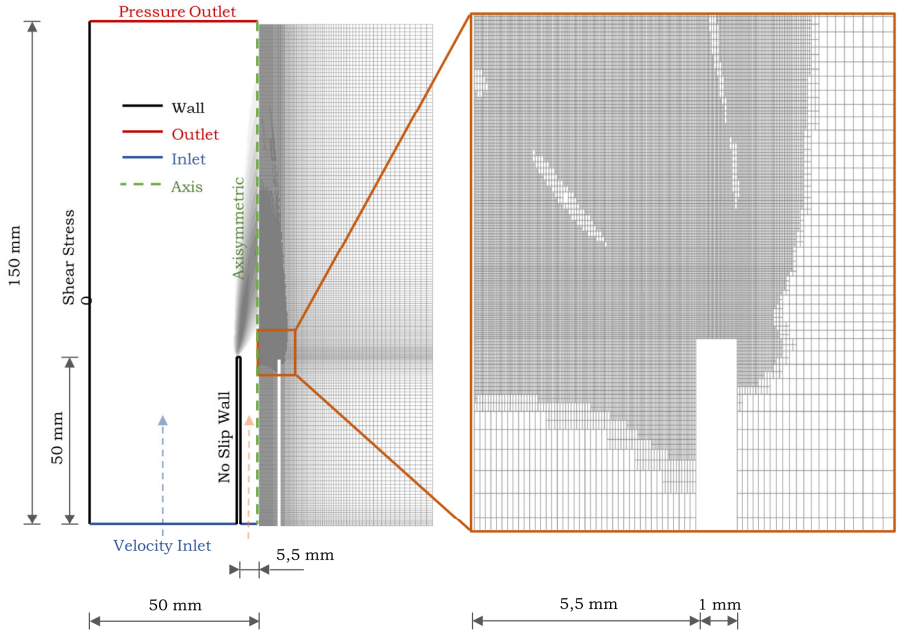

Fig. 1 2-D axisymmetric computational domain, boundary conditions, and refined computational mesh.

Mesh refinements were next carried out by mesh adaptions based on gradients of specific gaseous chemical species mass fractions scaled by their maximum field value [54]. The values for the scaled gradients of acetylene (C_2H_2) and hydroxyl (OH) mass fractions both corresponded to 0.01. These values were chosen to refine the flame reactive zone shown in Fig. 1. Adapting the computational mesh based on these two chemical species allowed an adequate mesh refinement on both fuel and oxidizer sides of the flame. Mesh coarsening was not performed in this work. Finally, mesh independence analyses were carried out accounting for one and two levels of refinement, comparing the concentration profiles of minor chemical species present in soot formation and evolution processes, i.e., C_2H_2, OH, and HCCO. The first level of mesh refinement consisted of approximately 50,000 elements, with the smallest element being about 60 μm in size. The second level of refinement in turn featured around 90,000 elements and the smallest element was about 30 μm in size. Maximum discrepancies found between the results with the initial mesh and the one with the first level of refinement were about 50 K for temperature and 20% for OH molar concentration. Additionally, the maximum discrepancies between the meshes with the first and second levels of refinement was only 3 K for temperature and 0.2% for [OH]. Thus, the mesh considered for the simulations performed here has one level of refinement only.

3.2 Solver and Numerical Schemes

The set of transport equations governing the reacting flow in this work was solved using the CFD (computational fluid dynamics) software ANSYS Fluent (Release 23.1). Chemistry models used here included the NBP [37] and KM2 [5] chemical kinetic mechanisms, implemented through the ANSYS Fluent Chemkin package. The stiff chemistry was solved using the Chemkin CFD solver, considering ideal gas formulations and average-mixture diffusion. The DOM model used in this work was discretized in a 4x4 angular grid, corresponding to a total of 64 directions, which, according to a previous work [50], provides a reasonable resolution. Soot models, MOMIC, and DSM transport equations were implemented through user-defined scalars (UDS). Following previous works [39,55], three (3) additional transport equations, each of them corresponding to a particular low-order statistical moment, were employed in the MOMIC model, whereas

thirty (30) transport equations, each of them corresponding to a soot volume section, were used in the DSM one. As highlighted in Section 3.3, the diffusion parameters and source terms for these models were implemented through user-defined functions (UDF). Regarding numerical schemes, a coupled method was used, with a second-order scheme utilized for the remaining transport equations. Finally, under-relaxation factors (URF) were used in the implementation of the soot models studied here to contribute to the stability and convergence of the numerical simulations. Specifically, URF values of 0.8 and 0.5 were employed for MOMIC and DSM, respectively.

3.3 Soot Model Implementation

To either modify existing numerical models or to add new ones, ANSYS Fluent allows the creation and usage of user defined functions (UDF) based on C as programming language and predefined macros. For instance, additional transport equations can be constructed following the structure,

$$\nabla \cdot (\rho \vec{v})\, \varphi_k = \nabla \cdot (\Gamma_s \nabla \varphi_k) + S_{\varphi_k}\,, \tag{11}$$

where φ_k is the transported scalar, Γ_s the diffusivity, and S_{φ_k} the transport equation source term. The particular soot models accounted for in this work have been implemented using these software features. The diffusion coefficient used by default in ANSYS Fluent's MOMIC model is the one employed for turbulent flames, defined as the ratio between the effective diffusion coefficient and the turbulent Prandtl number (μ_{eff}/σ_t). So, in this work, besides the modification introduced in the diffusion coefficient to properly model laminar flames, the evaluation of model parameters, such as the steric factor and sticking coefficient, and the selection of the chemical gas-phase species participating in the soot models source terms, were carried out through UDF. More specifically, to fully implement the soot models, user-defined scalars (UDS) were used to define the number of additional transport equations solved in the numerical simulations carried out here. In addition, the diffusion coefficient D_s and the source terms for each of the transport equations specified in Eqs. (2) and (6) were defined separately in different UDF. Following Roy et al. [56], to avoid solution divergence issues when using the MOMIC model, a limiting threshold for its oxidation source term was utilized to ensure the monotonicity of the statistical moments. This threshold for the ratio between moments M1/M0 was set to 32 here, which corresponds to the minimum number of carbon atoms

in an incipient soot particle. In addition, following the work described in [57], the DSM model source terms were linearized to both improve solution stability and avoid negative sectional volume fractions. The modification of radiation properties was also implemented through a UDF, where the soot absorption coefficient was defined according to Eq. (9).

Similarly, sink and source terms for the chemical species mass fractions consumed and generated during the soot formation and evolution processes were also considered via UDF. Finally, to monitor and post-process the implemented model variables and parameters, user defined memories (UDM) were also employed within the UDF.

As highlighted in the ANSYS Fluent Customization Manual (Release 23.1), the equations transported here were solved in a sequential order. First, the mass and momentum transport equations were computed, followed by the solution of the species mass fractions and energy equations. UDF source terms related to these equations, for instance species sinks and source terms, were called next. The additional transport equations, including UDS, were then solved. Finally, properties including those defined via UDF were updated accordingly.

4 Results and Discussions

The main results obtained in this work, in terms of chemical species mass fractions and molar concentrations, flame temperature, and soot volume fraction, are presented and discussed in this section. The influence on the referred results of chemical kinetic mechanisms and soot models are particularly assessed. Soot precursors are also analyzed in the final part of this section.

4.1 Chemical Kinetic Mechanisms Related Results

As highlighted in Section 2.3, two gas-phase chemical kinetic mechanisms, NBP and KM2, have been used in this work. Thus, this section compares, in terms of chemical gaseous species concentrations, the results obtained with these two kinetic mechanisms. The set of results discussed in this section corresponds to those obtained using the more detailed models evaluated in this work, the DSM soot model and the DOM radiation one. The chemical species considered for comparison purposes here are the ones present in the soot models assessed in this work and that are available in both NBP and KM2 kinetic

mechanisms. The distributions and peak values of these species are crucial to assess the differences between the two kinetic mechanisms, and to identify the possible source of discrepancies in the soot levels that could be obtained when using these kinetic mechanisms.

Accordingly, Fig. 2 shows molar concentrations of aromatic species A1, A2, and A4, which correspond to benzene, naphthalene, and pyrene, respectively. These aromatic species selected from the PAH species pool are illustrated here because they are the most frequently used PAH when modeling soot inception and condensation, as described in Eqs. (7) and (8). From Fig. 2 it can be seen that discrepancies between the molar concentration fields obtained with the two mechanisms increase as the aromatics become larger. In particular, the largest discrepancies are related with the pyrene molar concentration fields. Specifically, from Fig. 2(c), the field obtained using NBP shows a higher molar concentration in a flame region farther away from the burner, whereas the KM2 pyrene field shows a peak at a lower height above the burner. Notice as well that the discrepancies in the peak values, which are about 32%, 82%, and 94% for A1, A2, and A4, respectively, also increase as the PAH molecules become larger.

(a)

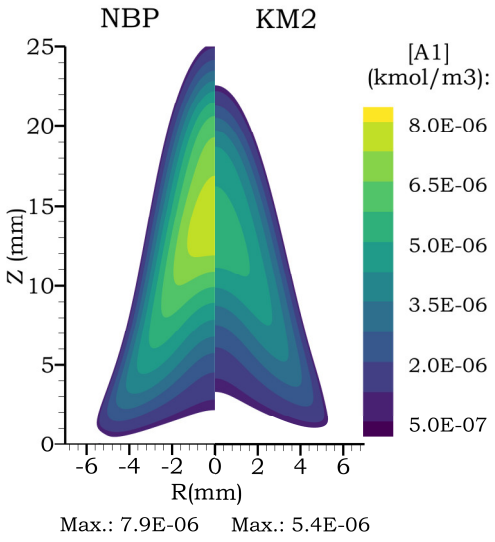

(b)

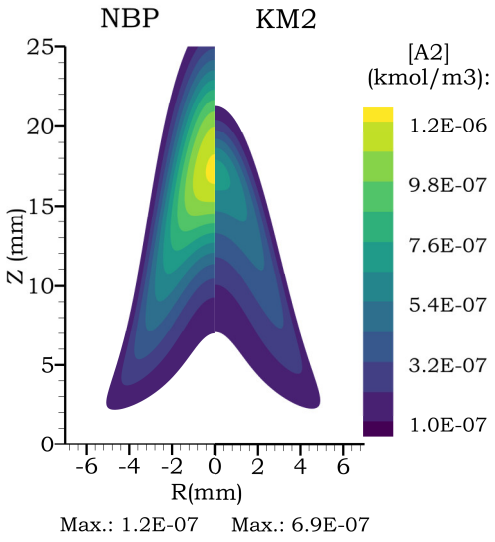

(c)

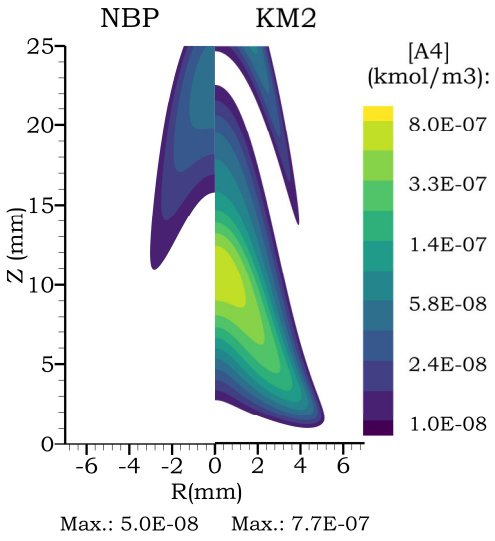

Fig. 2 Molar concentrations (kmol/m^3) obtained using the NBP and KM2 chemical kinetic mechanisms. (a) benzene (A1), (b) naphthalene (A2), and (c) pyrene (A4).

Similarly, Fig. 3 shows the molar concentration of the chemical species C_2H_2 and OH often assumed to control the soot evolution mechanisms of surface growth and oxidation, respectively. From this figure it can be observed first that the chemical species fields obtained using these two mechanisms seem to be quite similar. A closer look at Fig. 3(a) indicates however that the C_2H_2 peak values obtained with the studied mechanisms present discrepancies of about 18%. Contrarily, regarding the OH molar concentration, the associated peak values are almost indistinguishable, which suggests a high similarity between both kinetic mechanisms in the flame oxidizer rich region.

(a) (b)

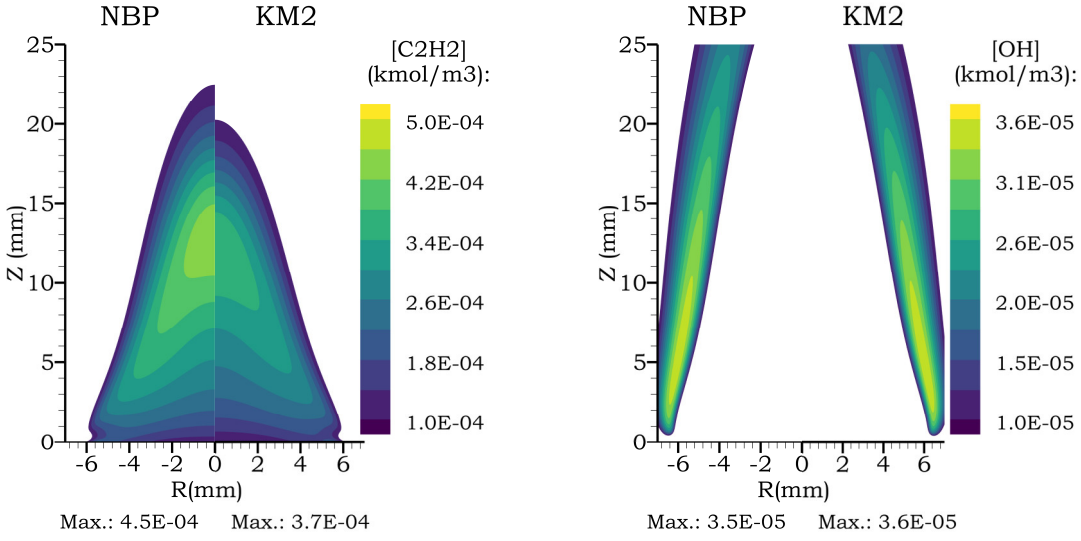

Fig. 3 Molar concentrations (kmol/m^3) obtained using the NBP and KM2 chemical kinetic mechanisms. (a) C_2H_2 and (b) OH.

The observed discrepancies between the results obtained using the NBP and KM2 kinetic mechanisms are somehow expected because they describe the pathways to PAH growth in different ways. For instance, the formation and consumption of A4 is described by 6 reactions in the NBP mechanism [37], whereas in the KM2, 34 reactions are directly associated with the formation of A4 [5]. Selecting among the two chemical kinetics mechanisms based on the concentration of the individual aromatic species would require measurements that, to the best of the authors knowledge, are unavailable for the particular flame studied here. However, the results in this section suggest that, depending on the chemical kinetic mechanism employed for this particular flame configuration, the use of relatively large PAH species in soot modeling would indeed lead to different soot levels.

4.2 Soot Modeling Related Results

Temperature and soot volume fraction related results obtained using the two detailed soot models accounted for here are first discussed in this section. This is complemented with soot production rates corresponding to the different soot formation and evolution mechanisms accounted for. In the numerical simulations performed to obtain the numerical results discussed in this section, the most detailed chemistry and radiation models accounted for in this work, the KM2 kinetic mechanism and the DOM radiation model, have been utilized along with the two soot models considered here. Notice that KM2 is considered to be more detailed than NBP since the number of chemical pathways and aromatic species is larger.

4.2.1 Temperature and Soot Volume Fraction

The experimental results obtained by Jerez et al. [32] are used here as a reference to compare the temperature and soot volume fraction (SVF) numerical ones obtained in this work using the studied detailed soot models, namely the method of moments with interpolative closure (MOMIC) and the discrete sectional method (DSM). Additionally, previous numerical results obtained with a sectional method model [32] are also included here for comparison purposes. Notice that temperature and SVF profiles are discussed here because soot particles effectively absorb and emit radiation, which has a strong

impact on flame temperature. SVF in turn allows analyzing the soot distribution in the flame. Following previous works [32], the experimental flame height (H) is defined here as the maximum axial (Z) position along the flame centerline where the band emission related to CH* chemiluminescence is observed. For the flame configuration studied here, the experimental flame height corresponds to 31.60 mm. Thus, the radial temperature and soot profiles shown in this section, at a normalized height of Z/H = 0.6, correspond to a Z (axial) position of 18.96 mm. Note that the maximum height for which measurements are available is Z = 25 mm.

Accordingly, Fig. 4 shows the temperature profiles obtained with the MOMIC and DSM soot models and those available [32]. As shown in Fig. 4(a), both MOMIC and DSM soot models reproduce the experimental centerline profile relatively well, with the profile obtained with DSM model being closer to the experimental one. Discrepancies over the centerline between the experimental peak values and the numerical ones are about 58 K and 2 K, for the MOMIC and DSM, respectively, which are within the flame temperature measurement uncertainty of 290K [32]. From Fig. 4(b) it is observed in turn that, relative to the experimental data, the temperature radial profiles obtained numerically here are slightly shifted to a higher radial position, being the MOMIC profile the furthest away from the experimental curve. Discrepancies between the experimental and numerical temperature peak values along the radial profile are 25 K and 59 K, for the MOMIC and DSM models, respectively. Additionally, it is observed from Fig. 4 (a) and (b) that, when compared to previous numerical results obtained using a sectional soot model, but with different gas phase chemical kinetic and radiation models [32], both axial and radial temperature profiles obtained with the DSM evaluated here are in better agreement with the experimental data.

(a) (b)

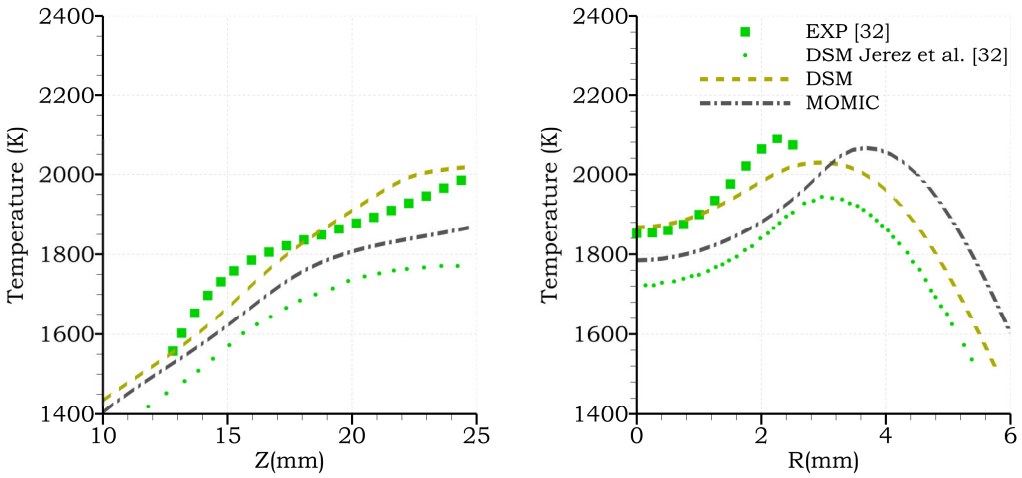

Fig. 4 Temperature profiles (a) along the flame centerline Z and (b) over a radial direction R at the position Z/H=0.6. Square symbols correspond to the experimental data [32], whereas dash-dot, dash, and dot lines correspond to numerical results.

Similarly, Fig. 5 shows the axial and radial profiles of soot volume fraction obtained experimentally and from the MOMIC and DSM numerical simulations carried out. Fig. 5(a) indicates that none of the detailed soot models properly predict the amount of soot formed along the flame centerline. However, among all the evaluated models, the DSM leads to a SVF peak value that is the closest to the experimental one. Compared to the experimental SVF peak value along the flame centerline, both DSM and MOMIC models exhibit discrepancies of approximately 1.6 and 2.3 ppm, respectively. These discrepancies correspond to SVF underestimations of 39 % and 56%, respectively, which exceed the experimental uncertainty of 30% [32]. Additionally, Fig. 5(b) shows that the SVF MOMIC radial profile is shifted to a higher radial position, whereas the DSM model correctly predicts the SVF peak position along the radial direction evaluated here. These results underscore that the soot volume fraction predictions heavily depend on the soot model employed. It is worth noticing here that the two soot models studied in this work use different empirical parameters and specific formulations for the soot associated mechanisms, which may account for the differences observed in the obtained results. The obtained numerical results also indicate that, for the type of flame configuration considered here, the DSM model predicts soot formation and evolution more accurately. However, the amount of soot generated over the center of the flame is underpredicted even with this model, so there is still room for further improvements.

(a) (b)

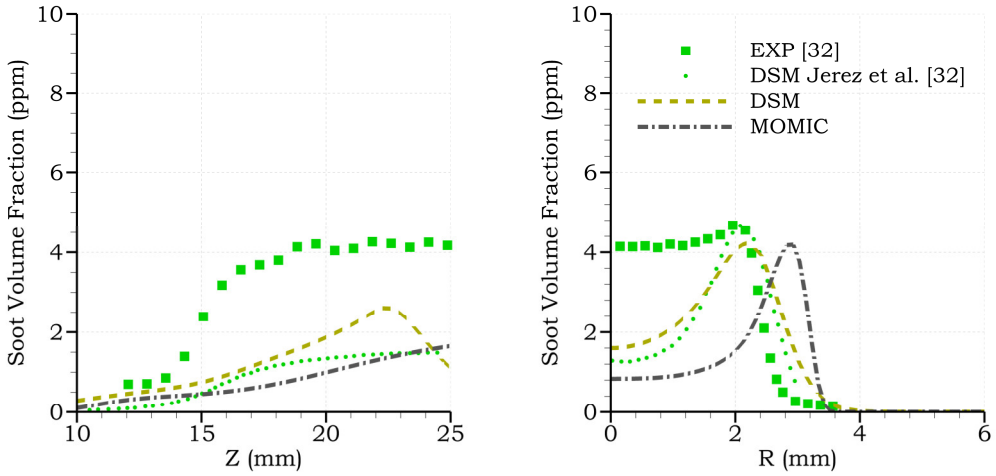

Fig. 5 Soot volume fraction profiles (a) along the flame centerline Z and (b) over a radial direction R at Z/H=0.6. Square symbols correspond to the experimental data [32], whereas dash-dot, dash, and dot lines correspond to numerical results.

4.2.2 Soot Production Rates

Both to gain further insight on the different behaviors reported in Section 4.2.1 and to characterize qualitatively and quantitatively the different soot formation and evolution mechanisms as source terms (Eqs. (3) and (7)), soot production rates are analyzed in this section. Like in Section 4.2.1, both MOMIC and DSM soot models along the KM2 kinetic mechanism are employed here. Accordingly, from left to right, Fig. 6(a) shows the soot production rates for the DSM model corresponding to inception, condensation, and surface growth, and the sink rates associated with oxidation. Fig. 6(b) shows the same soot production rates for MOMIC, except for condensation. It is possible to observe first from Fig. 6 the way in which the different soot formation and evolution mechanisms prevail in different regions of the flame. That is, inception and condensation are more important around the inner part of the flame, whereas surface mechanisms, i.e., surface growth and oxidation, are more important along the flame outer part. It is also worth noticing here the different magnitudes of the soot production rates. For the DSM model, surface growth and condensation are of the same order of magnitude, whereas soot inception is about three orders of magnitude smaller. Similarly, for the MOMIC model, surface growth and oxidation are of the same order of magnitude, whereas inception is one to two orders of magnitude smaller. This means that, in both soot models, most of the final soot mass produced comes from the soot mechanisms occurring at the particle

surface. Notice as well that, although inception may initially appear to be insignificant for soot mass production, this is not necessarily the case. Indeed, inception determines the number of soot particles that are initially formed and therefore plays a crucial role in the amount of soot that is observed.

Further analyses near the centerline of the contour plots shown in Fig. 6 indicate that the peak axial positions for the DSM rates are approximately at Z=16 mm for inception, Z=17 mm for condensation, Z=22 mm for surface growth, and Z=24 mm for oxidation. Conversely, the peak axial positions for the MOMIC rates are located at axial positions of 11, 28, and 30 mm for inception, surface growth, and oxidation, respectively. These differences in the peak axial positions may explain why the SVF values along the flame centerline discussed in Section 4.2.1 (Fig. 5(a)) differ for the two soot models. Indeed, for the DSM model, the position where the surface growth mechanism starts to decrease and the oxidation peaks (around an axial position of Z=22 to 24 mm) is similar to the position where the SVF starts to decrease along the flame centerline (Z=23 mm). Additionally, when comparing the two surface growth contours, it is observed that the one corresponding to the MOMIC model extends over a higher axial position. This mechanism may also increase the soot volume fraction values, which could also explain why the MOMIC model predicts an SVF profile that peaks at a radial position higher than both the experimental data and the DSM results (Fig. 5(b)).

(a)

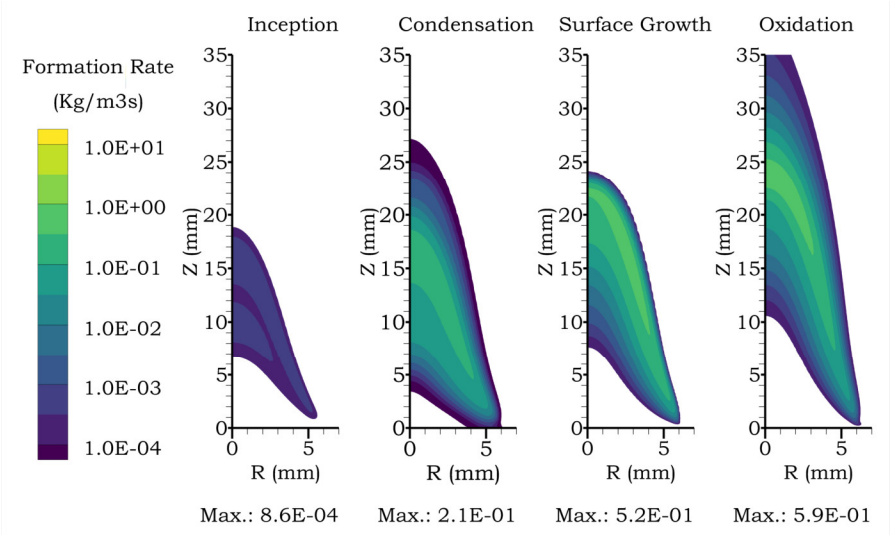

(b)

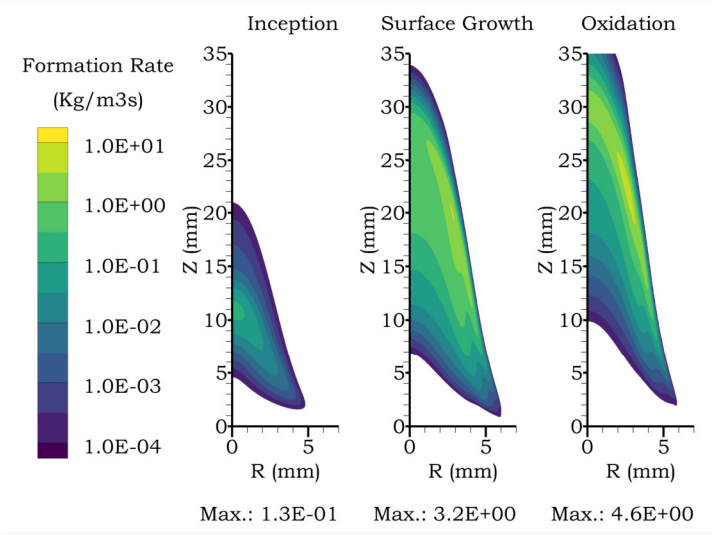

Fig. 6 Distribution of soot production rates (kg/m^{3}s) obtained using both (a) DSM and (b) MOMIC soot models.

4.3 Soot Precursors Analysis

In this section, to assess their influence on soot formation, PAH considered as precursors to soot formation are analyzed. First, following [32], PAH grouped by their number of rings are compared to planar laser induced fluorescence (PLIF) experimental measurements. Then the PAH are compared with each other in terms of their relative contribution to the soot inception rate [29]. The results shown in this section were obtained using the KM2 chemical kinetic mechanism and the DSM soot model.

Since direct measurements of individual PAH concentrations are not available for the studied flame, PAH groups are instead associated with a detected PLIF signal measurement at a characteristic wavelength [32]. Specifically, PAH groups containing 1, 2 and 3 aromatic rings are associated with the signals detected at 340 nm. In turn, signals at 400 nm are associated with PAH groups containing 3 and 4 aromatic rings. Accordingly, the PAH group R3 in Table 2 has been assigned to both 340 nm and 400 nm signals. Finally, the PLIF signal at 550 nm is associated with 5-ring aromatic molecules. Notice that each PAH group here consists of the most abundant PAH molecules found for the flame configuration utilized here, which are summarized in Table 2.

Table 2. PAH groups and chemical species.

PAH Group	Formula
R1	A1, $A1C_2H$, $A1C_2H_3$, $C_6H_5CH_2$
R2	A2, $A2C_2H$, C_9H_8, C_9H_7
R3	A3, A2R5, $A3C_2H$
R4	A4, A3R5, PYC_2H, CHRYSEN
R5	BAPYR, BEPYREN, A4R5

Accordingly, Fig. 7 (a), (b) and (c) show axial profiles of the normalized PLIF measurements and normalized sum of mass fractions obtained numerically (NUM) of each PAH group corresponding to wavelengths of 340, 400 and 550 nm, respectively. Notice that each profile is normalized by the maximum field value at each wavelength [32]. In addition, Fig. 8 (a) and (b) show radial profiles of normalized measurements and numerical results corresponding to wavelengths 340 and 400 nm, respectively. Notice, that the radial profiles shown here are located at a normalized height of Z/H = 0.3, corresponding to a Z position of 9.48 mm. From this set of results, it can be first observed that, overall, the numerical results obtained here are in good agreement with the experimental data.

From Fig. 7 (a), although the numerical simulation performed here reproduces the normalized peak position at about Z = 10 mm, it fails to reproduce the slope of the decreasing part of the curve. As it can be seen from Fig. 8 (a) as well, the largest difference found corresponds to the numerical radial profile at 340 nm, where the curve is shifted to a higher radial position. From figures 7 (a), (b) and (c) it can also be seen that the numerical results obtained here have a similar behavior to those also obtained numerically by Jerez et al. [32], that used a different chemical kinetic mechanism, i.e. the DLR [58]. Therefore, along the centerline the influence of the choice of the gas phase kinetic mechanism is important for the high molecular weight PAH only. However, Fig 8 (a) and (b) indicate that the opposite is observed for the radial PAH behavior. The present analysis suggests that the original proposal [32] of grouping aromatics and assigning specific PLIF emission wavelengths to them also holds for the KM2 chemical mechanism, as it did for the DLR one used in the referred work.

(a)

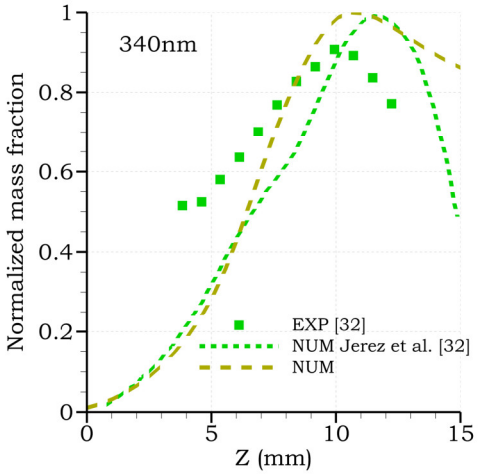

(b)

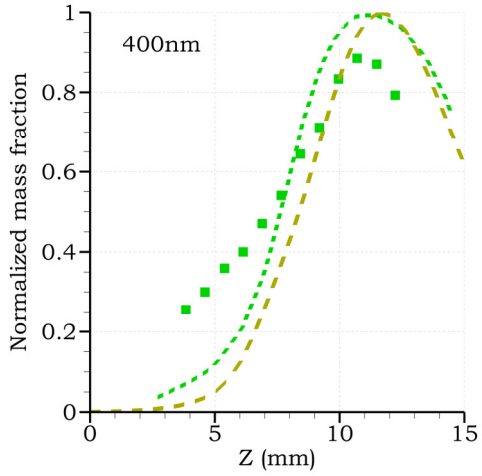

(c)

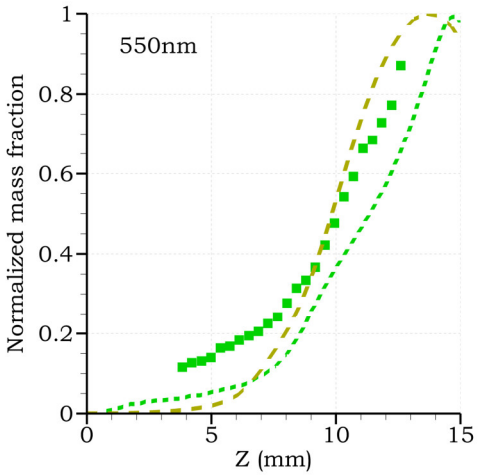

Fig. 7 Normalized mass fraction axial profiles for wavelengths (a) 340 nm (b) 400 nm and (c) 550 nm. Square symbols correspond to the experimental data [32], whereas dash, and dot lines correspond to numerical results.

(a)

(b)

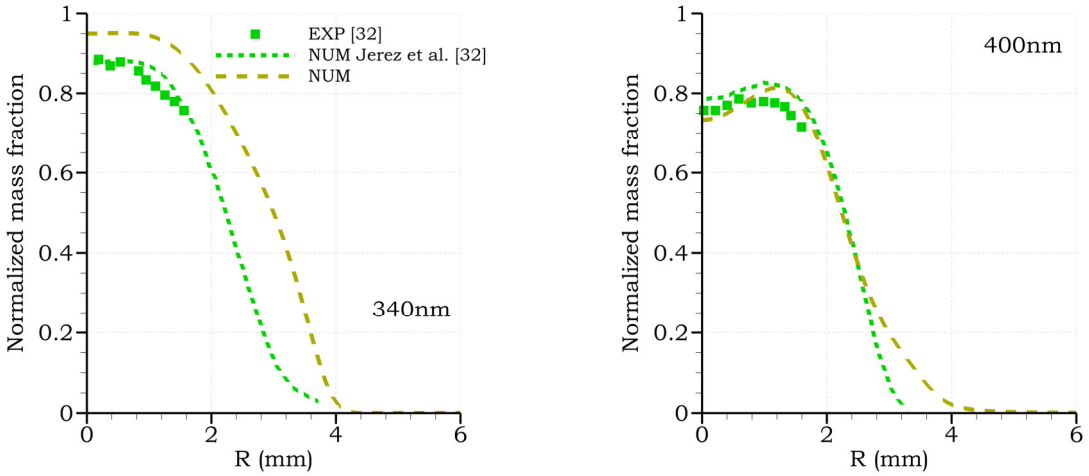

Fig. 8 Normalized mass fraction radial profiles at Z/H = 0.3 for wavelengths (a) 340 nm and (b) 400 nm. Square symbols correspond to the experimental data [32], whereas dash, and dot lines correspond to numerical results.

To extend the present analysis and thus further explore the relative PAH contribution to soot inception, Fig. 9 shows the contribution of PAH to the soot inception rate along the flame centerline. From this figure it is noticed that, at lower HAB (heights above the burner), pyrene (A4) is the PAH species that produces (through inception) the largest amount of soot, with contributions up to 85%. As the flame develops, the influence on soot inception of naphthalene (A2) and acenaphthylene (A2R5) increases. Indeed, first A2 reaches a maximum contribution to inception of 66% and then A2R5 accounts for 70% of the inception rate. Fig. 9 also highlights that larger PAH molecules, such as A4R5, PYC2H, BAPYR, and A7, have little impact on soot formation for this type of flame configuration. For instance, at a HAB of 20 mm (along the flame centerline), these PAH molecules reach a maximum contribution to the soot inception rate of only 13%. Additionally, Fig. 10 shows the PAH contribution to soot inception rate along a radial direction (HAB = 2 mm). For this particular height, it can be seen as well that, close to the centerline, A4 accounts for most of the inception rate, and as the flame expands most of the inception rate is mainly due to both A2 and A2R5.

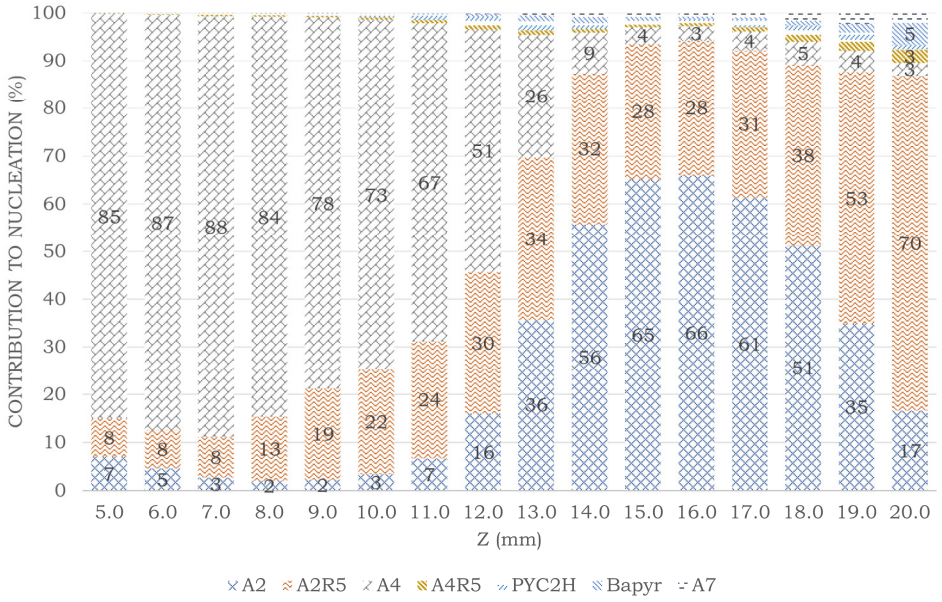

Fig. 9 PAH normalized contribution to soot inception rate over the flame centerline.

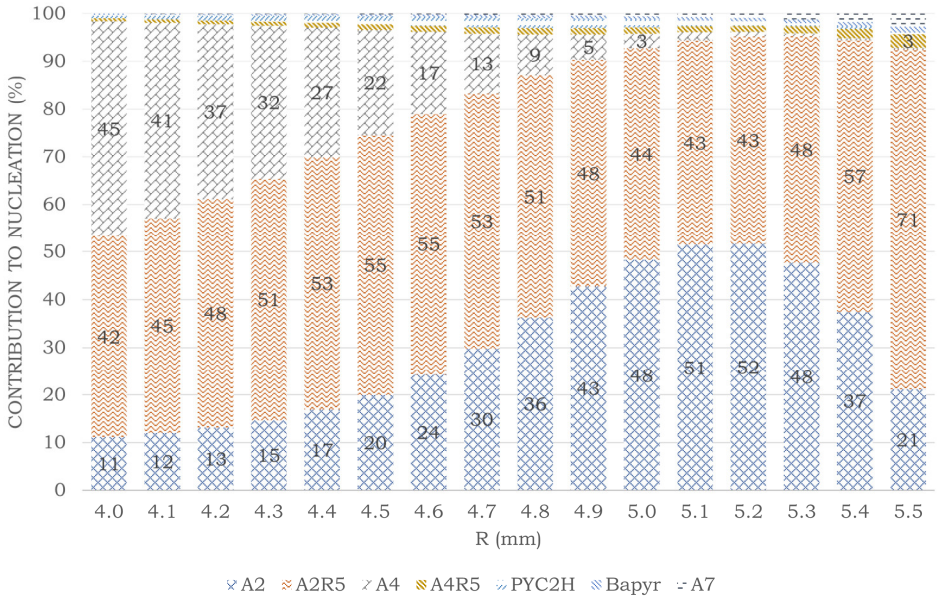

Fig. 10 PAH normalized contribution to soot inception rate over a radial direction at the position Z = 2 mm.

Given this relative contribution to soot inception, and to examine the role of three different PAH groups as soot precursors, Fig. 11 shows the corresponding soot volume fraction profiles along the flame centerline and along a radial direction. To obtain these

results, three numerical simulations were carried out considering different groups of PAH in the inception and condensation processes, defined in Eqs. (8) and (10). The PAH considered for this analysis are listed in Table 1, which are grouped according to their size [29]: (i) two to seven-ringed PAH (A2-A7), (ii) two to five-ringed PAH (A2-A4R5), and (iii) two to three-ringed PAH (A2 and A2R5). The results shown in Fig. 11 emphasizes that, excluding A5-A7 PAH from the group of soot precursor species, the amount of soot formed decreases by 0.02% only. In addition, when A4 and A4R5 are also excluded, the amount of soot formed decreases by 0.2%. These findings further confirm the observations made from the results shown in Fig. 9, where two to three-ringed PAH molecules, namely naphthalene and acenaphthylene, account for most of the soot generated by soot inception and condensation processes when the KM2 mechanism is used. These results also highlight that a complete soot inception formulation must indeed contain PAH of different sizes, mainly those with two to four aromatic rings. And that considering, for instance, only one of these PAH for the soot inception process could lead to an even further underprediction of SVF peak values.

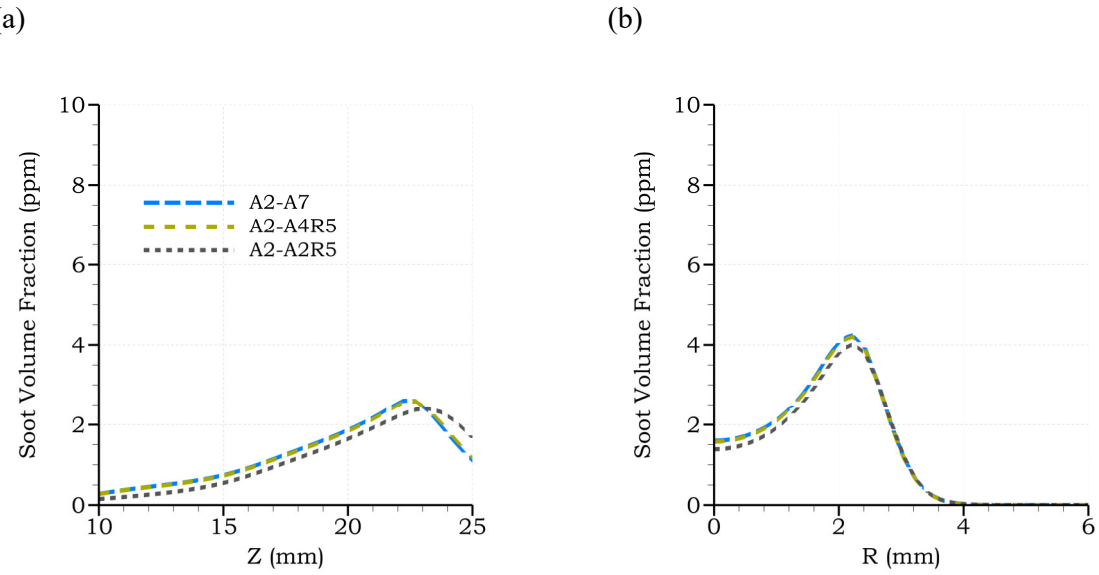

Fig. 11 Influence of soot precursors on soot volume fraction profiles (a) along the flame centerline Z and (b) over a radial direction R at Z/H = 0.6. Long dash, dash, and dot lines correspond to PAH groups with (i) two to seven, (ii) two to four and (iii) two to three aromatic rings, respectively.

5 Conclusions

In this work, two detailed soot models (MOMIC and DSM) were evaluated in laminar flames and the obtained results were compared with available experimental data. As part of the assessments carried out here, first, the NBP and KM2 chemical kinetic mechanisms were compared to each other accounting for the main chemical species taking part in soot formation and evolution processes, namely C_2H_2, OH, A1, A2, and A4. For relatively small species like C_2H_2 and OH, it was observed that the results obtained with both mechanisms are similar, but, as the studied species grow in molecular size, the discrepancies between the mechanisms related results increase. The relative discrepancies in peak molar concentrations obtained with the two evaluated kinetic mechanisms were indeed about 32%, 82%, and 94% for A1, A2, and A4, respectively. These discrepancies may come from the different chemical species and reaction pathways accounted for in each mechanism, which suggest that using different kinetic mechanisms in soot modeling would indeed produce different soot fields.

Regarding soot modeling, the numerical results obtained here showed that, in terms of temperature profiles, both models can reproduce the experimental data within the uncertainty range. SVF results showed in turn that the numerical predictions carried out with both detailed soot models over the flame centerline are not in good agreement with the magnitude of soot measured experimentally. Indeed, discrepancies of about 2.3 and 1.6 ppm were obtained in this case with the MOMIC and DSM models, respectively. It also was observed that, although both soot models capture the magnitude of the soot generated over a measured radial profile, the SVF profile obtained with the MOMIC model was shifted to a radial position, whereas the DSM one correctly reproduced the experimental maximum value. From these results, it is concluded that the DSM model reproduces better the soot experimental data for this flame. Nonetheless, to properly reproduce the amount of soot generated over the flame centerline, this DSM models needs further improvements, which is underscored by the assessment of the rates of the soot associated mechanisms. Indeed, inception and condensation are important in the central region of the flame, whereas surface growth dominates over the flame wing. This suggest that the soot underestimation over the flame centerline carried out by the soot models studied here may be originated from the underestimation of the inception and condensation source terms, which in turn depend on the PAH precursors concentration and a sticking coefficient.

Finally, the influence of different soot precursors on soot formation was evaluated by means of their contributions to the soot inception rate. From the results obtained in the referred assessments, it can be concluded that relatively small-sized PAH, ranging from naphthalene (A2) to pyrene (A4), are the PAH that impact the most on soot formation. More specifically, contributions of A4 were found to be more significant at lower heights above the burner, whereas A2 and A2R4 were found to be more impactful downstream as the flame develops. Maximum contributions of A2, A2R5, and A4 to the soot inception rate were 66%, 70%, and 85%, respectively, whereas the maximum summed contribution of PAH with five (A4R5) to seven (A7) aromatic rings accounted for only 13% of the inception rate. SVF evaluations considering different PAH groups in the inception formulation also confirmed that A2 and A2R5 account for most of the soot generated by PAH. The detailed models used here can be used to predict soot for different laminar flames. Nevertheless, the sticking coefficient, that relates to the PAH collision efficiency, may have to be fine-tuned, as may also the steric factor.

6 Acknowledgements

This work has been supported by CONCYTEC-FONDECYT (PROCIENCIA) (Peru), Contract No. 415-2019-2019-FONDECYT. During this work Luís Fernando Figueira da Silva was on leave from the Pontificia Universidade Catolica de Rio de Janeiro (PUC-Rio, Brazil).

7 Conflict of Interest Statement

The authors declare that they have no known competing financial interests or personal relationships that could have appeared to influence the work reported in this paper.

8 References

[1]R. Niranjan and A.K. Thakur, The toxicological mechanisms of environmental soot (black carbon) and carbon black: Focus on Oxidative stress and inflammatory pathways, Front. Immunol. 8 (2017).

[2]T. Bourdrel, M.A. Bind, Y. Béjot, O. Morel and J.F. Argacha, *Effets cardiovasculaires de la pollution de l'air*, Arch. Cardiovasc. Dis. 110 (2017), pp. 634–642.

[3]C.M. Long, M.A. Nascarella and P.A. Valberg, Carbon black vs. black carbon and other airborne materials containing elemental carbon: Physical and chemical distinctions, Environ. Pollut. 181 (2013), pp. 271–286.

[4]M. Kholghy, M. Saffaripour, C. Yip and M.J. Thomson, *The evolution of soot morphology in a laminar coflow diffusion flame of a surrogate for Jet A-1*, Combust. Flame 160 (2013), pp. 2119–2130.

[5]Y. Wang, A. Raj and S.H. Chung, A PAH growth mechanism and synergistic effect on PAH formation in counterflow diffusion flames, Combust. Flame 160 (2013), pp. 1667–1676.

[6]P. Selvaraj, P.G. Arias, B.J. Lee, H.G. Im, Y. Wang, Y. Gao et al., *A computational study of ethylene-air sooting flames: Effects of large polycyclic aromatic hydrocarbons*, Combust. Flame 163 (2016), pp. 427–436.

[7]T. Zhang, L. Zhao, M.R. Kholghy, S. Thion and M.J. Thomson, Detailed investigation of soot formation from jet fuel in a diffusion flame with comprehensive and hybrid chemical mechanisms, Proc. Combust. Inst. 37 (2019), pp. 2037–2045.

[8]M.E. Mueller, G. Blanquart and H. Pitsch, *Hybrid Method of Moments for modeling soot formation and growth*, Combust. Flame 156 (2009), pp. 1143–1155.

[9]N.A. Eaves, Q. Zhang, F. Liu, H. Guo, S.B. Dworkin and M.J. Thomson, *CoFlame: A refined and validated numerical algorithm for modeling sooting laminar coflow diffusion flames*, Comput. Phys. Commun. 207 (2016), pp. 464–477.

[10] Q. Zhang, H. Guo, F. Liu, G.J. Smallwood and M.J. Thomson, Modeling of soot aggregate formation and size distribution in a laminar ethylene/air coflow diffusion flame with detailed PAH chemistry and an advanced sectional aerosol dynamics model, Proc. Combust. Inst. 32 (2009), pp. 761–768.

[11] A. Veshkini, S.B. Dworkin and M.J. Thomson, Understanding soot particle size evolution in laminar ethylene/air diffusion flames using novel soot coalescence models, Combust. Theory Model. 20 (2016), pp. 707–734.

[12] S. Valencia, S. Ruiz, J. Manrique, C. Celis and L.F.F. da Silva, *Soot modeling in turbulent diffusion flames: review and prospects*, J. Brazilian Soc. Mech. Sci. Eng. 43, 219 (2021).

[13] M.F. Modest and D.C. Haworth, *Radiative Heat Transfer in Turbulent Combustion Systems: Theory and Applications*, 1st ed.Springer International Publishing, 2016.

[14] T.F. Smith, Z.F. Shen and J.N. Friedman, *Evaluation of coefficients for the weighted sum of gray gases model*, J. Heat Transfer 104 (1982), pp. 602–608.

[15] F. Cassol, R. Brittes, F.H.R. França and O.A. Ezekoye, Application of the weighted-sum-of-gray-gases model for media composed of arbitrary concentrations of H2O, CO2 and soot, Int. J. Heat Mass Transf. 79 (2014), pp. 796–806.

[16] F. Liu, J.L. Consalvi, P.J. Coelho, F. Andre, M. Gu, V. Solovjov et al., The impact of radiative heat transfer in combustion processes and its modeling – with a focus on turbulent flames, Fuel 281 (2020), pp. 118555.

[17] E. Quadarella, J. Guo and H.G. Im, A consistent soot nucleation model for improved prediction of strain rate sensitivity in ethylene/air counterflow flames, Aerosol Sci. Technol. 56 (2022), pp. 636–654.

[18] R.S. Mehta, D.C. Haworth and M.F. Modest, An assessment of gas-phase reaction mechanisms and soot models for laminar atmospheric-pressure ethylene-air flames, Proc. Combust. Inst. 32 (2009), pp. 1327–1334.

[19] A. Wick, M. Frenklach and H. Pitsch, Systematic assessment of the Method of Moments with Interpolative Closure and guidelines for its application to soot particle dynamics in laminar and turbulent flames, Combust. Flame 214 (2020), pp. 450–463.

[20] T. Blacha, M. Di Domenico, P. Gerlinger and M. Aigner, Soot predictions in premixed and non-premixed laminar flames using a sectional approach for PAHs and soot, Combust. Flame 159 (2012), pp. 181–193.

[21] A. Dasgupta, S. Roy and D.C. Haworth, Detailed computational modeling of laminar and turbulent sooting flames, in ACM International Conference Proceeding Series, 2014.

[22] Y. Wang, A. Raj and S.H. Chung, Soot modeling of counterflow diffusion flames of ethylene-based binary mixture fuels, Combust. Flame 162 (2015), pp. 586–596.

[23] J. Guo, P. Selvaraj, H.G. Im, Y. Tang and V. Raman, An analysis of soot formation pathways in laminar coflow ethylene flames at higher pressures, AIAA Scitech 2020 Forum (2020).

[24] H.A. Michelsen, M.B. Colket, P.E. Bengtsson, A. D'Anna, P. Desgroux, B.S. Haynes et al., *A review of terminology used to describe soot formation and evolution under combustion and pyrolytic conditions*, ACS Nano 14 (2020), pp. 12470–12490.

[25] G. Blanquart and H. Pitsch, *A joint volume-surface-hydrogen multi-variate model for soot formation*, in *Combustion Generated Fine Carbonaceous Particles*, H. Bockhorn, A. D'Anna, A.F. Sarofim and H. Wang, eds., KIT Scientific Publishing, 2009, pp. 437–463.

[26] H. Jin, J. Guo, T. Li, Z. Zhou, H.G. Im and A. Farooq, Experimental and numerical study of polycyclic aromatic hydrocarbon formation in ethylene laminar co-flow diffusion flames, Fuel 289 (2021), pp. 119931.

[27] J.W. Martin, M. Salamanca and M. Kraft, *Soot inception: Carbonaceous nanoparticle formation in flames: Soot inception*, Prog. Energy Combust. Sci. 88 (2022), pp. 100956.

[28] P. Selvaraj, P.G. Arias, B.J. Lee, H.G. Im, Y. Wang, Y. Gao et al., *A computational study of ethylene-air sooting flames: Effects of large polycyclic aromatic hydrocarbons*, Combust. Flame 163 (2016), pp. 427–436.

[29] J. Guo, Y. Tang, V. Raman and H.G. Im, Numerical investigation of pressure effects on soot formation in laminar coflow ethylene/air diffusion flames, Fuel 292 (2021), pp. 120176.

[30] A. Jerez, J.L. Consalvi, A. Fuentes, F. Liu and R. Demarco, Soot production modeling in a laminar coflow ethylene diffusion flame at different Oxygen Indices using a PAH-based sectional model, Fuel 231 (2018), pp. 404–416.

[31] C. Lou, Z. Li, Y. Zhang and B.M. Kumfer, Soot formation characteristics in laminar coflow flames with application to oxy-combustion, 227 (2021), pp. 371–383.

[32] A. Jerez, J.J. Cruz Villanueva, L.F. Figueira da Silva, R. Demarco and A. Fuentes, *Measurements and modeling of PAH soot precursors in coflow ethylene/air laminar diffusion flames*, Fuel 236 (2019), pp. 452–460.

[33] V. Chernov, M.J. Thomson, S.B. Dworkin, N.A. Slavinskaya and U. Riedel, *Soot formation with C1 and C2 fuels using an improved chemical mechanism for PAH growth*, Combust. Flame 161 (2014), pp. 592–601.

[34] M. Frenklach, *Method of moments with interpolative closure*, Chem. Eng. Sci. 57 (2002), pp. 2229–2239.

[35] S.P. Roy, *Aerosol-dynamics-based soot modeling of flames*, Ph.D Thesis. The Pennsylvania State University, 2014.

[36] C.A. Hoerlle, Modelling of soot formation based on the Discrete Sectional Method: CO2 effects and coupling with the FGM technique, Ph.D Thesis. Universidade Federal do Rio Grande do Sul, 2020.

[37] K. Narayanaswamy, G. Blanquart and H. Pitsch, *A consistent chemical mechanism for oxidation of substituted aromatic species*, Combust. Flame 157 (2010), pp. 1879–1898.

[38] USC Mech Version II. High-Temperature Combustion Reaction Model of H2/CO/C1-C4 Compounds. Available at http://ignisuscedu/USC_Mech_II.htm.

[39] A. Wick, M. Frenklach and H. Pitsch, Systematic assessment of the Method of Moments with Interpolative Closure and guidelines for its application to soot particle dynamics in laminar and turbulent flames, Combust. Flame 214 (2020), pp. 450-463.

[40] A. Abdelgadir, I.A. Rakha, S.A. Steinmetz, A. Attili, F. Bisetti and W.L. Roberts, *Effects of hydrodynamics and mixing on soot formation and growth in laminar coflow diffusion flames at elevated pressures*, Combust. Flame 181 (2017), pp. 39–53.

[41] S. Rigopoulos, *Modelling of Soot Aerosol Dynamics in Turbulent Flow*, Flow, Turbul. Combust. 103 (2019), pp. 565–604.

[42] L. Zimmer and F. Pereira, *Limitations of simplified models to predict soot formation in laminar flames*, J. Brazilian Soc. Mech. Sci. Eng. 42 (2020), .

[43] J. Appel, H. Bockhorn and M. Frenklach, Kinetic modeling of soot formation with detailed chemistry and physics: Laminar premixed flames of C2 hydrocarbons, Combust. Flame 121 (2000), pp. 122–136.

[44] M. Frenklach and H. Wang, Detailed mechanism and modeling of soot particle formation, in Soot Formation in Combustion. Springer Series in Chemical Physics, H. Bockhorn, ed., Springer, Berlin, Heidelberg, 1994, pp. 165–192.

[45] S. Ruiz, R.S. Valencia Ramírez, C. Celis and L.F. Figueira da Silva, *Parametric Study of Empirical Constants Used in Soot Formation Models Based on*

*Interpolative Closure Methods of Moment*s, in 19th Brazilian Congress of Thermal Sciences and Engineering, 2022.

[46] K. Netzell, H. Lehtiniemi and F. Mauss, Calculating the soot particle size distribution function in turbulent diffusion flames using a sectional method, Proc. Combust. Inst. 31 I (2007), pp. 667–674.

[47] F. Gelbard, Y. Tambour and J.H. Seinfeld, *Sectional representations for simulating aerosol dynamics*, J. Colloid Interface Sci. 76 (1980), pp. 541–556.

[48] S.S. Sazhin, An approximation for the absorption coefficient of soot in a radiating gas., Manuscript, Fluent Eur. Ltd (1994).

[49] P.B. Taylor and P.J. Foster, *Some Gray Gas Weighting Coefficients for CO2-H2O-Soot Mixtures*, Int. J. Heat Mass Transf. 18 (1974), pp. 1331–1332.

[50] L. Mazzei, S. Puggelli, D. Bertini, D. Pampaloni and A. Andreini, *Modelling soot production and thermal radiation for turbulent diffusion flames*, Energy Procedia 126 (2017), pp. 826–833.

[51] F. França, A. Ziemniczak, L.G. Pires Rodrigues, L. Domingues Lemos and F. Pereira, *Comparison of different WSGG approaches in numerical simulation of a non-premixed turbulent methane-air flame*, 16th Brazilian Congr. Therm. Sci. Eng. (2018).

[52] H. Guo, F. Liu, G.J. Smallwood and Ö.L. Gülder, The flame preheating effect on numerical modelling of soot formation in a two-dimensional laminar ethylene-air diffusion flame, Combust. Theory Model. 6 (2002), pp. 173–187.

[53] N. Lopes Junqueira, L. da Costa Ramos and L.F. Figueira da Silva, *Reduced order model of diffusion flames based on multi-scale data from detailed CFD: the impact of preprocessing*, J. Brazilian Soc. Mech. Sci. Eng. 46 (2024), .

[54] L. da Costa Ramos, L.F. Figueira da Silva, F. Di Meglio and V. Morgenthaler, *Modeling of Pulsating Inverted Conical Flames : a Numerical Instability Analysis*, Combust. Theory Model. 26 (2022), pp. 260–288.

[55] M.D. Smooke, R.J. Hall, M.B. Colket, J. Fielding, M.B. Long, C.S. McEnally et al., *Investigation of the transition from lightly sooting towards heavily sooting co-flow ethylene diffusion flames*, Combust. Theory Model. 8 (2004), pp. 593–606.

[56] S.P. Roy, P.G. Arias, V.R. Lecoustre, D.C. Haworth, H.G. Im and A. Trouvé, *Development of high fidelity soot aerosol dynamics models using method of moments with interpolative closure*, Aerosol Sci. Technol. 48 (2014), pp. 379–391.

[57] S. V. Patankar, *Numerical Heat Transfer and Fluid Flow*, 1st ed.Hemisphere Publishing Corporation, 1980.

[58] N. Slavinskaya, A. Mirzayeva, R. Whitside, J.H. Starke, M. Abbasi, M. Auyelkhankyzy et al., *A modelling study of acetylene oxidation and pyrolysis*, Combust. Flame 210 (2019), pp. 25–42.